

# Evolution of the X-ray Profiles of Poor Clusters from the XMM-LSS Survey

Abdulmonem Alshino,<sup>1\*</sup> Trevor Ponman,<sup>1</sup> Florian Pacaud<sup>2</sup> and Marguerite Pierre<sup>3</sup>

<sup>1</sup>*School of Physics and Astronomy, The University of Birmingham, Birmingham B15 2TT, UK.*

<sup>2</sup>*Argelander-Institut für Astronomie, University of Bonn, Auf dem Hügel 71, 53121 Bonn, Germany.*

<sup>3</sup>*DAPNIA/SaP CEA Saclay, 91191 Gif sur Yvette, France.*

Accepted XXXX XXXX XX. Received XXXX XXXX XX; in original form XXXX XXXX XX

## ABSTRACT

A sample consisting of 27 X-ray selected galaxy clusters from the *XMM-LSS* survey is used to study the evolution in the X-ray surface brightness profiles of the hot intracluster plasma. These systems are mostly groups and poor clusters, with temperatures 0.6–4.8 keV, spanning the redshift range 0.05 to 1.05. Comparing the profiles with a standard  $\beta$ -model motivated by studies of low redshift groups, we find 54% of our systems to possess a central excess, which we identify with a cuspy cool core. Fitting  $\beta$ -model profiles, allowing for blurring by the XMM point spread function, we investigate trends with both temperature and redshift in the outer slope ( $\beta$ ) of the X-ray surface brightness, and in the incidence of cuspy cores. Fits to individual cluster profiles and to profiles stacked in bands of redshift and temperature indicate that the incidence of cuspy cores does not decline at high redshifts, as has been reported in rich clusters. Rather such cores become more prominent with increasing redshift.  $\beta$  shows a positive correlation with both redshift and temperature. Given the  $\beta$ - $T$  trend seen in local systems, we assume that temperature is the primary driver for this trend. Our results then demonstrate that this correlation is still present at  $z \gtrsim 0.3$ , where most of our clusters reside.

**Key words:** galaxies: clusters: general - galaxies: X-ray.

## 1 INTRODUCTION

Clusters of galaxies, as the largest virialised gravitationally-bound products of the process of hierarchical structure formation, are powerful probes for both testing cosmological models and tracing structural evolution (e.g., Voit 2005). One of the most important properties of galaxy clusters is their mass. Since cluster mass cannot be directly observed, it is studied indirectly through observables such as X-ray radiation emitted by the intracluster medium (ICM) which represents 80% of the total baryonic component of galaxy clusters at  $z=0$  (Ettori et al. 2004) and accounts for about 10% of the total (including dark) mass content of clusters (Sarazin 1986). The study of the ICM can provide important insights into the evolution and dynamics of cluster and their member galaxies.

Observationally, there are two distinct classes of clusters: cool core (CC) clusters with dense gaseous core regions in which gas temperature drops inwards, and non-cool core (NCC) clusters with shallower core profiles which often exhibit more internal structure (e.g., Jones & Forman 1984; Ota & Mitsuda 2004; Peres et al. 1998 and Schuecker et al. 2001). Cool core clusters have sharply

peaked X-ray emission at their centres due to the rise in central gas density which accompanies the central cooling. However, the gas is not observed to cool to very low temperatures at the rates naively expected from the observed core X-ray luminosities, and a consensus has now emerged that this is due to the effects of feedback from a central active galactic nucleus, which limits the effects of cooling through processes which are still not very well understood. For reviews of cool cores in clusters, see for example, Fabian 1994, Donahue & Voit 2004 and Peterson & Fabian 2006.

In the local Universe, some studies have found that nearly two thirds of clusters have cool cores (e.g. Peres et al. 1998, White et al. 1997 and Vikhlinin et al. 2007). However, other studies gave different values: Edge, Stewart & Fabian (1992) found a CC fraction as high as 90%, while the results of Chen et al. (2007) indicated that 49% of local clusters host cool cores. These differences relate to both the selection of the cluster sample, and the way in which cool cores are identified within them.

The evolution of cooling within clusters provides an important probe of the history of cosmic feedback (Voit 2005). At intermediate redshifts ( $z \approx 0.15 - 0.4$ ), Bauer et al. (2005), using a sample of 38 X-ray-luminous clusters, found that cool cores appeared still to be common, with an incidence nearly identical to that in lumi-

\* E-mail: alshino@star.sr.bham.ac.uk

nous low-redshift clusters. Consequently, they suggested that heating and cooling processes must have stabilised in massive clusters since  $z \sim 0.4$ .

At higher redshifts, Vikhlinin et al. (2007) reported that the fraction of clusters with cuspy X-ray cores dropped from  $\sim 70\%$  at  $z \sim 0$  to  $\sim 15\%$  at  $z > 0.5$ . Santos et al. (2008) compared the fraction of clusters with non-cool cores, moderate cool cores and strong cool cores in nearby ( $0.143 \leq z \leq 0.3$ ) and high redshift ( $0.7 \leq z < 1.4$ ) clusters. These authors detected a significant fraction of clusters harbouring moderate cool cores out to  $z=1.4$ , similar to the fraction in their low-redshift sample. However, they noticed an absence of clusters with strong-cool cores at redshift  $z > 0.7$ .

Regarding the spatial distribution of the ICM, Cavaliere & Fusco-Femiano (1976) introduced the  $\beta$ -model profile, motivated by the distribution expected for an isothermal plasma in hydrostatic equilibrium with a virialised mass distribution. Although it is now known that the gas is rarely isothermal, the  $\beta$ -model is generally found to give a reasonable representation of X-ray surface brightness profiles (e.g. Neumann & Arnaud 1999). However, an additional central component is usually required to fit the inner regions of CC clusters (e.g. Pratt & Arnaud 2002), and detailed studies of surface brightness profiles of clusters extending to large radii have shown that the logarithmic slope continues to increase slowly towards larger radii (e.g. Vikhlinin, Forman & Jones 1999, Croston et al. 2008 and Maughan et al. 2008). It is less clear whether this progressive steepening is also present in galaxy groups. For example, Rasmussen & Ponman (2004) traced the surface brightness out to  $R_{500}$  in two rich groups and found them to be well fitted by simple  $\beta$ -models the whole way.

For  $\beta$ -model fits, the  $\beta$  parameter, which characterises the outer slope of the surface brightness profile, has a value of  $\approx 2/3$  for rich clusters (Jones & Forman 1984) and lower values for poor clusters and galaxy groups (Finoguenov, Reiprich & Böhringer 2001, Helsdon & Ponman 2000 and Horner et al. 1999). Several studies have shown that  $\beta$  has a mild positive trend with the average temperature of the ICM in nearby clusters (Vikhlinin, Forman & Jones 1999, Croston et al. 2008 and Maughan et al. 2008) and that the value in poorer galaxy groups is lower (i.e. flatter surface brightness slope) than that in clusters (Osmond & Ponman 2004). In terms of evolution, a study of Chandra data for 115 clusters spanning the range  $0.1 < z < 1.3$  by Maughan et al. (2008) shows some indication that the  $\beta$ - $T$  correlation is weaker for clusters at  $z > 0.5$ .

Low-mass galaxy clusters or groups, with ICM temperatures less than 2-3 keV, play an important role in the evolution of galactic systems because they lie at a transition between the field environment and rich cluster environments, and also because non-gravitational processes have a larger impact in groups than in rich clusters (e.g., Zabludoff & Mulchaey 1998, Ponman, Sanderson & Finoguenov 2003 and Sun et al. 2009). However, these poor systems, and in particular the evolution of their properties, have received rather little attention. This is mainly due to the difficulty in detecting and studying them, especially at large redshifts, due to their faint X-ray emission and small complement of galaxies.

For these reasons, research on the evolution of galactic systems in the regime of groups and poor clusters has only started recently, as a result of improvements in observing capabilities in both the X-ray and optical. By comparing optically-selected systems at  $0.3 \leq z \leq 0.55$  with nearby groups, Wilman et al. (2005) showed that the fraction of group members undergoing significant star for-

mation increases strongly with redshift out to  $z \sim 0.45$ . However, the study of X-ray selected groups by Jeltema et al. (2007) showed a contrary result: they did not observe significant evolution in the morphology or star formation of the galaxy populations in their  $0.2 < z < 0.6$  groups compared to low-redshift X-ray luminous groups. They argued that this discrepancy could be due to different selection methods, since optically-selected systems are typically lower in mass and contain more spiral galaxies and therefore a stronger evolution in the galaxies is expected. They also found that their moderate redshift groups had galaxy populations similar to clusters at the same redshift; in particular, a large fraction of early-type galaxies and a low fraction of galaxies with significant star formation. However, in contrast to the situation in low redshift X-ray bright groups, a significant fraction of these intermediate redshift groups were found (Mulchaey et al. 2006, Jeltema et al. 2007) to have no bright early-type galaxy at the centre of the X-ray emission, or to have a central galaxy with multiple nuclei. This was taken as evidence for the dynamical youth of many of these groups.

The small number of studies which have addressed the evolution in the X-ray properties of galaxy groups have found little convincing evidence for any. Jeltema et al. (2006), in a multiwavelength study of six galaxy groups and poor clusters at intermediate redshift (0.2-0.6), found that they appear to follow the scaling relations between luminosity, temperature, and velocity dispersion defined by low-redshift groups and clusters. This is also true (Jeltema et al. 2009) for three higher redshift poor clusters from the AEGIS survey. A study of evolution in the  $L$ - $T$  relation based on the present XMM-LSS cluster sample by Pacaud et al. (2007), taking into account the selection function of the survey, found that the range of models consistent with the data included self-similar evolution, and also (marginally) a no-evolution model. Finoguenov et al. (2007) extracted a larger sample of 72 clusters (mostly poor ones) from the XMM-Newton observations of the COSMOS field, and found no evidence for evolution in the luminosity function of these systems out to  $z \sim 1$ , though the quality of their data did not permit them to study the morphology of the X-ray emission.

Motivated by the the paucity of information available for the evolution of the ICM in the important environment of low-mass galaxy clusters, we aim in this study to shed light on the spatial distribution of the ICM in X-ray selected clusters covering a wide redshift range ( $z \sim 0 - 1$ ), paying special attention to trends in the slope and central cusps of the X-ray emission.

The paper is constructed as follows: in section 3.2, we describe the data and briefly introduce the properties of the cluster sample; then we describe the data reduction used to produce X-ray surface brightness profiles. In section 3.3, we present our results, starting with the individual cluster profiles, and then profiles of redshift-stacked and temperature-stacked clusters. In section 3.4, we discuss the implication of our results and compare them with other studies. Finally, in section 3.5, we summarise our conclusions.

Throughout this paper, we adopt the cosmological parameters from the five-year WMAP data presented by Hinshaw et al. (2009), namely:  $H_0 = 70.5 \text{ km s}^{-1} \text{ Mpc}^{-1}$ ,  $\Omega_m = 0.27$ ,  $\Omega_\Lambda = 0.73$ .

## 2 DATA

### 2.1 The sample

Our sample is based on the 29 Class 1 (C1) clusters from the X-ray Multi-Mirror Large-Scale Structure (XMM-LSS) survey. The

XMM-LSS C1 cluster sample is a well-controlled X-ray selected and spectroscopically confirmed cluster sample. The criteria used to select the members of this sample guarantee negligible contamination of point-like sources. The observations of the clusters were performed in a homogeneous way (10-20 ks exposures). For full details of the C1 sample, see Pacaud et al. (2007). Detailed information on the selection function of the C1 sample can be found in Pacaud et al. (2006).

The C1 sample is dominated by groups and poor clusters with temperatures of  $0.63 \leq kT \leq 4.80$  keV, spanning a redshift range  $0.05 \leq z \leq 1.05$ . Typically, we have a few hundreds X-ray counts for each cluster, with only a few having over a thousand detected photons. Two of the 29 clusters with less than 80 counts had to be excluded from our analysis because their data were inadequate for useful profiles to be extracted. The excluded clusters are XLSSC clusters 39 and 48. Hence our sample consists of 27 clusters. Cluster 47, with 81 counts, was a marginal case. We were unable to constrain a fit to its individual profile, but its data were included in the analysis of the stacked profiles. Key properties of the sample are presented in Table 1.

## 2.2 Data analysis

To construct the X-ray surface brightness profiles for each cluster, we used three X-ray FITS images, three exposure maps and one segmentation map, all produced using the production pipeline described in Pacaud et al. (2006). The images were taken by the MOS1, MOS2 and PN imagers on board the XMM-Newton satellite in the energy band [0.5-2.0] keV with exposure times ranging from 10 to 20 ks. The exposure maps are FITS images containing the vignetting-corrected exposure of the clusters as a function of the sky position. A single segmentation map, generated by SEXTRACTOR was used for each cluster to remove contaminating sources.

The right ascension (RA) and declination (Dec) values of the centres were determined as outlined in Pacaud et al. (2006). But when we examined the X-ray profiles of the clusters, some showed dips at the centre. For these clusters, we mosaicked the three images, smoothed the resulting image and took the coordinates of the pixel with the maximum photon counts and modified the cluster centre accordingly. The modified centres at most are only  $\sim 14$  arcseconds from the original values but remove the central dips in the profiles. The clusters with modified centres have XLSSC numbers: 50, 28, 40, 1, 47 and 5. The RAs and Decs in Table 1 are the modified centres and the original coordinates can be found in Table 1 in Pacaud et al. (2007).

Since the angular size of our clusters is small, background removal using a local estimate works well. The background was taken from an annulus extending from  $2 \times R_{500}$  to  $3 \times R_{500}$  about each cluster, where  $R_{500}$  is the radius within which the mean cluster mass density is 500 times the critical density of the Universe at the cluster redshift. As in Pacaud et al. (2007), the  $R_{500}$  values were calculated using

$$R_{500} = 0.388 \times T^{0.63} \times h_{70.5}(z)^{-1} \text{Mpc}, \quad (1)$$

where  $T$  is the ICM temperature in keV and  $h_{70.5}$  is the Hubble constant in units of  $70.5 \text{ kms}^{-1} \text{Mpc}^{-1}$ . This formula was originally derived from M-T relation of Finoguenov, Reiprich & Böhringer (2001).

Two background components were evaluated: the photon background component and the particle background component. These were separated using the fact that photons are vignettted, whilst particles are not. Hence the relationship between count rate

and effective area for pixels in the background annulus gives an estimate of the photon background component from the slope, and of the particle background component from the intercept.

Surface brightness profiles were extracted from a standard set of annuli (as a fraction of  $R_{500}$  to facilitate later stacking), extending to  $3 \times R_{500}$ . For each annulus we removed the particle background and computed the vignetting-corrected count rate (in ct/s/pix) and its error. The MOS1, MOS2 and PN profiles, generated in this way were then combined, and their errors added in quadrature. Profiles were extracted up to  $3 \times R_{500}$  where they flattened and reached the photon background values. The final column in Table 1 is the total X-ray counts within  $3 \times R_{500}$  after subtracting from it both the photon and the particle background.

The X-ray cameras on the XMM-Newton satellite have a point spread function (PSF) of  $\sim 6$  arcsec FWHM, see Strüder et al. (2001) and Turner et al. (2001). Correction for PSF blurring is important to avoid biased estimation of the parameters of the cluster's radial profile, especially, the core radius,  $r_{\text{core}}$ . We applied the PSF correction method used by Arnaud et al. (2002) (and described in detail therein) which analytically computes a photon redistribution matrix (RDM) based on the properties of the three XMM-Newton cameras and depends on the energy band used and off-axis angle between the centre of the camera and the cluster position. The PSF matrices for the three cameras were weighted by the source counts in each camera and combined to produce a matrix appropriate to the coadded profiles.

We fitted the surface brightness profile with a  $\beta$ -model (Cavaliere & Fusco-Femiano 1976)

$$S(r) = S_0 (1 + (r/r_{\text{core}})^2)^{-3\beta+0.5}, \quad (2)$$

where  $S_0$  is central brightness (cts/s/pix) and  $r_{\text{core}}$  is the core radius (in units of  $R_{500}$ ). The model was blurred with the PSF redistribution matrix, and fitted to the surface brightness data. The best values of  $r_{\text{core}}$  and  $\beta$  were estimated by computing the minimum  $\chi^2$  value on an adaptively refined  $r_{\text{core}}-\beta$  grid.  $1\sigma$  errors were computed for  $r_{\text{core}}$  and  $\beta$ , and  $1\sigma$ ,  $2\sigma$  and  $3\sigma$  error regions computed in the  $r_{\text{core}}-\beta$  plane for each fit.

As will be seen below, a number of systems show a central excess above the fitted  $\beta$ -model. Such a central cusp suggests the possible presence of a cool core. Since a central excess may distort the  $\beta$ -model fit, we attempted to fit a model with the central bin excluded, but given the limited statistical quality of our data, loss of the central bin resulted in poorly behaved fits in many cases. We therefore adopted the approach of fitting a  $\beta$ -model with core radius fixed at a value (as a fraction of  $R_{500}$ ) motivated by the observed profiles of local groups in which detailed modelling of the surface brightness has been possible. A central excess above this model then indicates the presence of a cuspy core.

The fixed value of the core radius we adopt as a canonical value for poor clusters is taken from Helsdon & Ponman (2000), who studied 24 X-ray-bright galaxy groups. For half of their sample they found that two-component  $\beta$ -models were required to give acceptable fits to the surface brightness distribution. The outer component represented the intragroup gas, whilst core emission could be distinguished by a clear shoulder in the profile in many cases, and was fitted by the inner  $\beta$ -model component. The median value of  $r_{\text{core}}$  for the outer component in the 12 clusters was found to be 60 kpc. Correcting to our value of  $H_0$ , this median  $r_{\text{core}}$  would be 42.6 kpc. The 12 systems in Helsdon & Ponman (2000) had an average temperature of 1.07 keV. To calculate this  $r_{\text{core}}$  as a fraction of  $R_{500}$ , we used the  $R_{500}(T)$  equation above, which gives

XLSSC number	R.A. (J2000)	Dec. (J2000)	Redshift	$kT$ (keV)	$r_{500}$ (Mpc)	$\beta$ Fitted $r_{\text{core}}$	$r_{\text{core}}/R_{500}$	$\beta$ Fixed $r_{\text{core}}$	Central Excess Factor ( $f_c$ )	Counts
11	36.5413	-4.9682	0.05	0.64	0.290	$0.45^{+0.03}_{-0.02}$	$0.08^{+0.03}_{-0.03}$	$0.47^{+0.01}_{-0.02}$	$1.14 \pm 0.14$	795
52	36.5681	-2.6660	0.06	0.63	0.285	$0.69^{+0.07}_{-0.05}$	$0.14^{+0.03}_{-0.02}$	$0.62^{+0.02}_{-0.01}$	$0.95 \pm 0.09$	561
21	36.2345	-5.1339	0.08	0.68	0.297	$0.65^{+0.27}_{-0.09}$	$0.04^{+0.03}_{-0.02}$	$1.34^{+0.29}_{-0.22}$	$1.04 \pm 0.12$	87
41	36.3777	-4.2391	0.14	1.34	0.440	$0.47^{+0.02}_{-0.01}$	$0.05^{+0.02}_{-0.01}$	$0.51^{+0.01}_{-0.01}$	$1.70 \pm 0.22$	656
50	36.4233	-3.1895	0.14	3.50	0.804	$0.78^{+0.06}_{-0.05}$	$1.12^{+0.09}_{-0.09}$	$0.37^{+0.02}_{-0.01}$	$0.59 \pm 0.07$	4387
35	35.9507	-2.8588	0.17	1.20	0.394	$0.44^{+0.05}_{-0.04}$	$0.13^{+0.07}_{-0.06}$	$0.42^{+0.02}_{-0.02}$	$0.67 \pm 0.37$	422
25	36.3531	-4.6776	0.26	2.00	0.533	$0.58^{+0.05}_{-0.04}$	$0.07^{+0.02}_{-0.02}$	$0.65^{+0.03}_{-0.02}$	$1.42 \pm 0.18$	683
44	36.1411	-4.2347	0.26	1.30	0.399	$1.37^{+4.48}_{-0.61}$	$0.63^{+0.25}_{-0.31}$	$0.50^{+0.03}_{-0.02}$	$1.02 \pm 0.41$	276
51	36.4982	-2.8265	0.28	1.20	0.518	$1.81^{+***}_{-0.84}$	$0.77^{+0.12}_{-0.31}$	$0.47^{+0.05}_{-0.03}$	$2.18 \pm 1.09$	160
22	36.9165	-4.8576	0.29	1.70	0.471	$0.57^{+0.02}_{-0.02}$	$0.04^{+0.01}_{-0.01}$	$0.71^{+0.02}_{-0.02}$	$1.46 \pm 0.16$	1234
27	37.0143	-4.8510	0.29	2.80	0.653	$0.70^{+0.10}_{-0.10}$	$0.40^{+0.13}_{-0.10}$	$0.45^{+0.02}_{-0.01}$	$0.86 \pm 0.23$	653
8	36.3370	-3.8015	0.30	1.30	0.396	$0.53^{+0.11}_{-0.07}$	$0.04^{+0.04}_{-0.03}$	$0.67^{+0.08}_{-0.06}$	$1.54 \pm 0.47$	160
28	35.9878	-3.0991	0.30	1.30	0.399	$0.43^{+0.08}_{-0.05}$	$0.08^{+0.09}_{-0.06}$	$0.45^{+0.04}_{-0.04}$	$3.65 \pm 1.42$	245
13	36.8586	-4.5380	0.31	1.00	0.340	$0.58^{+1.25}_{-0.14}$	$0.06^{+0.20}_{-0.05}$	$0.73^{+0.20}_{-0.12}$	$1.54 \pm 1.01$	120
18	36.0087	-5.0904	0.32	2.00	0.521	$0.94^{+0.76}_{-0.22}$	$0.19^{+0.14}_{-0.06}$	$0.68^{+0.04}_{-0.04}$	$1.02 \pm 0.27$	89
40	35.5272	-4.5431	0.32	1.60	0.442	$0.44^{+0.04}_{-0.02}$	$0.01^{+0.02}_{-0.01}$	$0.55^{+0.05}_{-0.04}$	$2.70 \pm 0.74$	223
10	36.8435	-3.3623	0.33	2.40	0.574	$0.57^{+0.08}_{-0.05}$	$0.08^{+0.05}_{-0.03}$	$0.61^{+0.03}_{-0.02}$	$1.94 \pm 0.35$	327
23	35.1894	-3.4328	0.33	1.70	0.457	$0.54^{+0.03}_{-0.03}$	$0.05^{+0.01}_{-0.01}$	$0.65^{+0.03}_{-0.03}$	$1.19 \pm 0.27$	394
6	35.4385	-3.7715	0.43	4.80	0.838	$0.68^{+0.03}_{-0.03}$	$0.19^{+0.02}_{-0.02}$	$0.570^{+0.003}_{-0.011}$	$0.84 \pm 0.09$	1394
36	35.5280	-3.0539	0.49	3.60	0.676	$0.60^{+0.06}_{-0.04}$	$0.08^{+0.03}_{-0.02}$	$0.67^{+0.03}_{-0.02}$	$1.37 \pm 0.22$	481
49	35.9892	-4.5883	0.49	2.20	0.493	$2.20^{+***}_{-0.92}$	$0.38^{+0.04}_{-0.13}$	$0.67^{+0.06}_{-0.05}$	$1.59 \pm 0.55$	157
1	36.2367	-3.8131	0.61	3.20	0.584	$0.62^{+0.05}_{-0.04}$	$0.11^{+0.02}_{-0.02}$	$0.62^{+0.02}_{-0.02}$	$2.25 \pm 0.30$	595
2	36.3844	-3.9200	0.77	2.80	0.493	$0.83^{+0.57}_{-0.18}$	$0.09^{+0.08}_{-0.04}$	$0.92^{+0.14}_{-0.11}$	$3.03 \pm 0.68$	136
47	35.5461	-2.6783	0.79	3.90	0.592					81
3	36.9098	-3.2996	0.84	3.30	0.518	$0.48^{+0.05}_{-0.04}$	$0.03^{+0.02}_{-0.02}$	$0.64^{+0.07}_{-0.05}$	$1.15 \pm 0.54$	193
5	36.7854	-4.3003	1.05	3.70	0.489	$2.42^{+***}_{-1.33}$	$0.33^{+0.05}_{-0.17}$	$0.80^{+0.13}_{-0.09}$	$2.46 \pm 0.94$	130
29	36.0172	-4.2251	1.05	4.10	0.524	$0.76^{+0.37}_{-0.16}$	$0.11^{+0.08}_{-0.05}$	$0.76^{+0.07}_{-0.06}$	$1.86 \pm 0.59$	233

**Table 1.** List of the properties of the 29 C1 galaxy clusters sample sorted according to their redshifts (Pacaud et al. 2007) with the fitted parameters of the 26 successfully constrained clusters. The  $\beta$  and  $r_{\text{core}}$  values in the seventh and eighth columns are for the  $\beta$ -model with both  $r_{\text{core}}$  and  $\beta$  freely fitted. The  $\beta$  values in the ninth column are for the  $\beta$ -model with fixed  $r_{\text{core}}=0.105 \times R_{500}$ . All errors are  $1\sigma$  errors. Clusters 47 failed to converge but its data were not excluded from the stacked analysis. The central excess factor,  $f_c$  (tenth column), is calculated by dividing the observed surface brightness by the predicted surface brightness (from the fitted model) for the innermost radial bin, that is  $0.05 \times R_{500}$ . If  $f_c$  is greater than 1 then this is considered as an indication that the cluster has a cool core and vice versa. The stars (\*\*\*) denote unconstrained errors.

$r_{\text{core}}=0.105 \times R_{500}$ . This value of  $r_{\text{core}}$  was therefore used in our fixed-core fits.

To quantitatively determine whether a profile of a cluster (or a stacked set of clusters) has a central brightness excess, and therefore a CC, we define the central excess factor ( $f_c$ ) as the ratio between the observed surface brightness and predicted surface brightness (from the fitted fixed-core model) for the innermost radial bin, at  $r = 0.05 \times R_{500}$ . If  $f_c$  is greater than 1 then this was considered as an indication that the cluster has a CC and vice versa. The error on  $f_c$  is derived simply from the error on the innermost surface brightness value. We checked the effects of excluding the central bin for the fixed-core fits. This has little effect on the fitted  $\beta$  value, but in cases where there is a central excess, it results in a somewhat lower normalisation for the fitted model, and hence a slightly (up to 10%) higher value of  $f_c$ .

### 2.3 Stacked profiles

The statistical quality of our individual profiles is limited, so we stacked the observed profiles of clusters with similar redshifts and temperatures, producing higher quality profiles which might highlight any trends with temperature or redshift.

Since each cluster has a different  $R_{500}$ , we extracted the pro-

files in fixed radial bins in units of  $R_{500}$  up to  $3 \times R_{500}$ . The range from  $(0-1) \times R_{500}$  was divided into 20 equally spaced bins, from  $(1-2) \times R_{500}$  into 15 equally spaced bins and the range from  $(2-3) \times R_{500}$  into 10 equally spaced bins. These different bin widths allow for the decline in flux with radius whilst keeping the inner bins sufficiently fine to resolve the core. This distribution of bins was chosen after some experimentation to obtain the best fit constraints.

Before the stacking, the profiles were multiplied by the scale factor:

$$\frac{1}{A \times B \times C}, \quad (3)$$

where

$$A = R_{500} \quad (4)$$

to account for the cluster line of sight depth,

$$B = \left( \frac{\rho_c(z)}{\rho_c(z=0)} \right)^2 \quad (5)$$

to correct for the change in critical density of the Universe and

$$C = (1+z)^{-4} \quad (6)$$

to eliminate the effect of cosmological dimming. The aim of the

scaling is to allow for the effects of variable cluster depth and for cosmological factors, so that all profiles would be similar (to within the rather weak temperature dependence of the X-ray emissivity) in the case where clusters are simple self-similar systems, evolving with the critical density of the Universe.

The profiles for each component cluster were then added bin by bin and their errors quadratically summed to generate a stacked profile. The photon background values for each cluster were scaled by the same factors as the source profiles, before being combined. This coadded photon background was then included in the fitted model as a fixed background level. The PSF redistribution matrices were weighted by the scaled count rate for each cluster before being combined to produce a composite matrix.

### 3 RESULTS

#### 3.1 X-ray surface brightness profiles of individual C1 clusters

Most individual C1 clusters profiles fit successfully with a free- $r_{\text{core}}$   $\beta$ -model, and nearly all have well-constrained fixed- $r_{\text{core}}$   $\beta$ -model fits. The profile of cluster 47, with only 81 counts, is the only one for which we could not achieve a useful  $\beta$ -model fit. For clusters 51 (160 counts), 49 (157 counts) and 5 (130 counts), although best fit models were obtained, the upper bound of the free- $r_{\text{core}}$   $\beta$  values were not constrained, and no  $r_{\text{core}}$ - $\beta$  contour plots could be produced.

The surface brightness profiles with fits and associated  $1\sigma$ ,  $2\sigma$  and  $3\sigma$  error contours for individual clusters with redshift ranges 0.05-0.17, 0.26-0.33 and 0.43-1.05 are shown in Fig. 1, 2 and 3 respectively, and numerical results are given in Table 1. The profile of cluster 50 is unusual; it has a remarkably large  $r_{\text{core}}$  value, of  $1.12 \times R_{500}$  (see Fig. 1), and an elongated spatial extension indicating a cluster in a state of merging, with a highly unrelaxed core.

Amongst the 26 clusters with constrained fixed- $r_{\text{core}}$  fits, 21 (81%) possess CCs according to the criterion outlined above (i.e.  $f_c > 1$ ), whilst the remaining five (19%) are non-cool core (NCC) ( $f_c < 1$ ) systems, as shown in Table 1. However, for some of these, the classification must be regarded as uncertain, since the error bar on  $f_c$  crosses unity. This is the case for 7 (from the 21) CC systems, and 2 (of the five) NCC clusters. Hence, at the  $1\sigma$  level, 54% (14 out of 26) of our clusters show a central excess in surface brightness which may indicate the presence of a cool core.

The median value of  $\beta$  for free- $r_{\text{core}}$  fits to the 26 clusters is 0.61. A similar median value ( $\beta=0.63$ ) is obtained from the fixed- $r_{\text{core}}$  fits. As for the  $r_{\text{core}}$ , its median value is  $0.08 \times R_{500}$ . As expected, this is rather smaller than the canonical value of  $0.105 \times R_{500}$  for the group scale component of the emission, due to the influence on the fits of cuspy cores in many systems.

#### 3.2 X-ray surface brightness profiles of redshift-stacked clusters

The C1 clusters span a redshift range of 0.05 to 1.05. To probe how the X-ray surface brightness profiles evolve with redshift, we divided the C1 sample into three redshift ranges: 0.05-0.17 (low- $z$ ), 0.26-0.33 (intermediate- $z$ ) and 0.43-1.05 (high- $z$ ). The low- $z$  set consists of 6 clusters with an average redshift of 0.11 and a temperature range from 0.63 to 3.50 keV (average 1.33 keV). Only one of these (cluster 50) has  $kT > 2$  keV. Twelve clusters fall in

the intermediate- $z$  stacked set, with average redshift and temperature of 0.30 and 1.69 keV respectively. The high- $z$  set contains 9 clusters spanning a redshift range 0.43 to 1.05 (average 0.72) and having temperatures from 2.20 to 4.80 keV (average 3.51 keV). The profiles and the error contours of the three stacked sets are presented in Fig. 4 and the fitted parameters for the free and fixed  $\beta$ -model fits with  $1\sigma$  errors are shown in the first three rows of Table 2.

The central excess factor,  $f_c$  is seen to increase with redshift; for the low- $z$  stack it is 1.30, increasing to 1.56 and 1.95 for the intermediate and high  $z$  systems respectively. Table 2 also shows that  $\beta$  (for both free and fixed  $r_{\text{core}}$  fits) increases with redshift, whilst the  $r_{\text{core}}$  values are essentially constant.

#### 3.3 X-ray surface brightness profiles of temperature-stacked clusters

The full temperature range of our C1 sample (0.63 to 4.80 keV) was divided into three subsets. The coolest set ( $0.63 \text{ keV} \leq kT \leq 1.34 \text{ keV}$ ) contains ten clusters with average  $kT=1.06$  keV and average  $z=0.20$ . There are nine clusters in the second set ( $1.60 \text{ keV} \leq kT \leq 2.80 \text{ keV}$ ) with averages  $kT=2.13$  keV and  $z=0.38$ , and the hottest set ( $3.20 \text{ keV} \leq kT \leq 4.80 \text{ keV}$ ) contains eight clusters with average temperature and redshift of 3.76 keV and 0.68 respectively. The stacked profiles and the associated  $1\sigma$ ,  $2\sigma$  and  $3\sigma$  contours are shown in Fig. 5 and the fitted parameter values in Table 2.

All three temperature-stacked sets show evidence for CCs, with  $f_c > 1$ . However,  $f_c$  does not show a monotonic trend with temperature as was the case for the redshift-stacked clusters. The intermediate-temperature set shows the strongest central excess, with  $f_c=2.17 \pm 0.28$ . Similarly, the  $\beta$  values, for both fixed and free  $r_{\text{core}}$  fits, do not show a monotonic trend across the full  $T$  range of our sample, although it is clear that the hotter systems ( $kT > 1.5$  keV) have  $\beta$  values significantly higher than the groups in our coolest bin. The core radius,  $r_{\text{core}}$  appears remarkably stable in these stacked clusters, fitting at a value  $0.07 \times R_{500}$ . This is also essentially the case for the redshift-stacked clusters, in which the high and low redshift stacks fitted at  $r_{\text{core}}=0.07 \times R_{500}$  whilst the intermediate-redshift stack gives  $r_{\text{core}}=0.06 \times R_{500}$ , which is the same within errors.

### 4 DISCUSSION

#### 4.1 X-ray surface brightness profiles of $z \sim 0.3$ clusters

Pacaud et al. (2007) show (see their Fig. 3) that the redshift distribution of the C1 clusters, which spans the redshift range 0.05 to 1.05, has a pronounced peak around  $z \sim 0.3$ . More than 40% (12 systems) of our clusters are concentrated in the relatively small redshift range  $0.26 \leq z \leq 0.33$ . The average temperature of these 12 clusters is 1.69 keV. Their average  $M_{500}$  is  $3.96 \times 10^{13} M_{\odot}$ . This puts them in the realm of groups or poor clusters. To our knowledge, this is the best sample of X-ray selected groups at  $z \sim 0.3$  studied to date, and hence our individual and stacked X-ray profiles of these clusters provide the best available X-ray profile of low-mass clusters at intermediate redshift, and should be useful for future comparative studies. The individual X-ray profiles with the  $r_{\text{core}}$ - $\beta$  contours for these cluster are shown in Fig. 2 and the stacked profile is the second panel in Fig. 4.

The free- $r_{\text{core}}$  fit to the stacked profile for these clusters gives  $\beta = 0.51$  (see Table 2, second row) which is

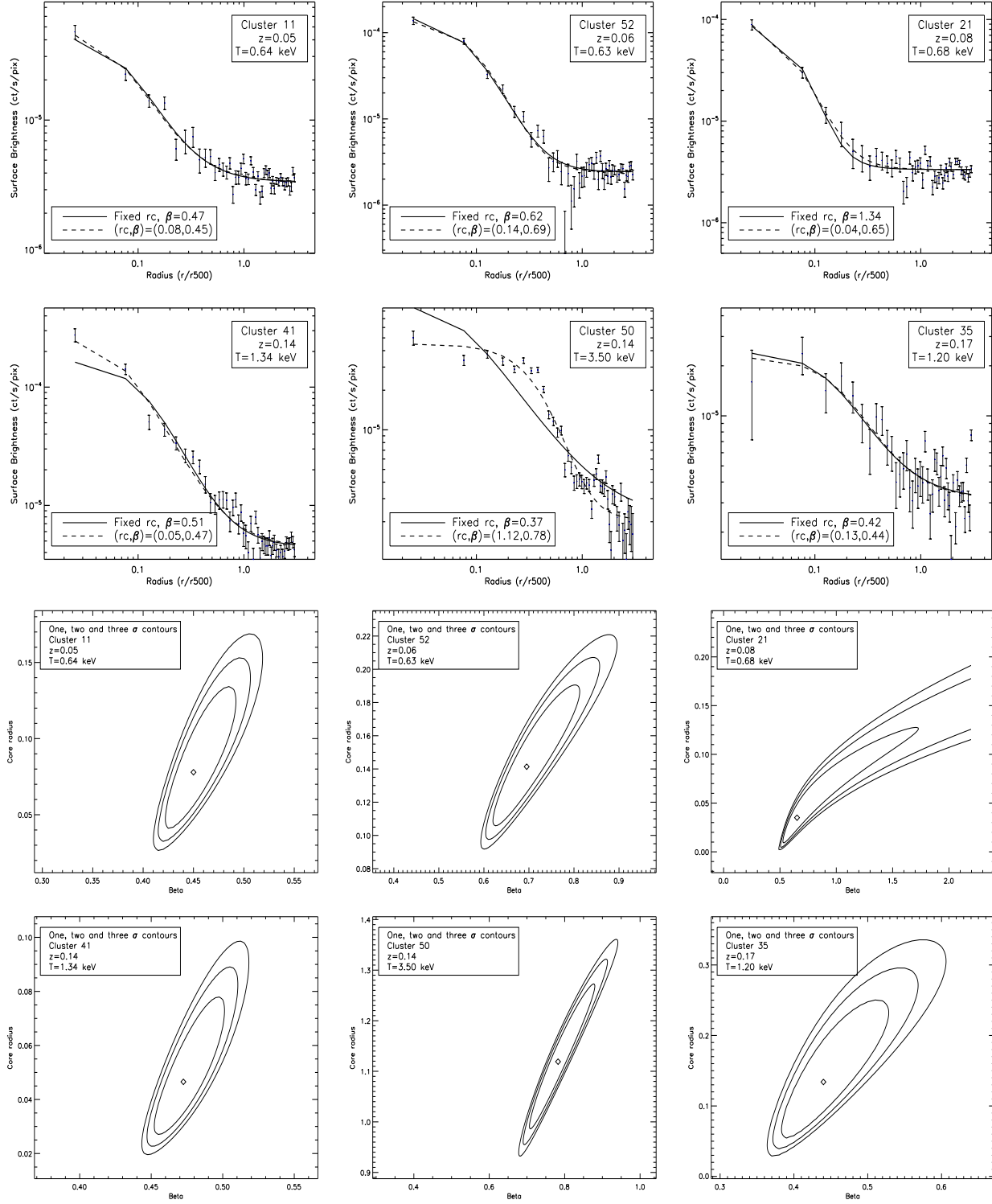


**Figure 1.** X-ray surface brightness profiles of the individual C1 clusters with redshift  $0.05 \leq z \leq 0.17$ , ordered according to redshift and the associated  $1\sigma$ ,  $2\sigma$  and  $3\sigma$  contours. The dashed lines are the fitted  $\beta$ -model profiles with both  $r_{\text{core}}$  and  $\beta$  freely fitted, while the solid lines are for the fitted profiles with free  $\beta$  and  $r_{\text{core}}$  fixed to  $0.105 \times R_{500}$ .

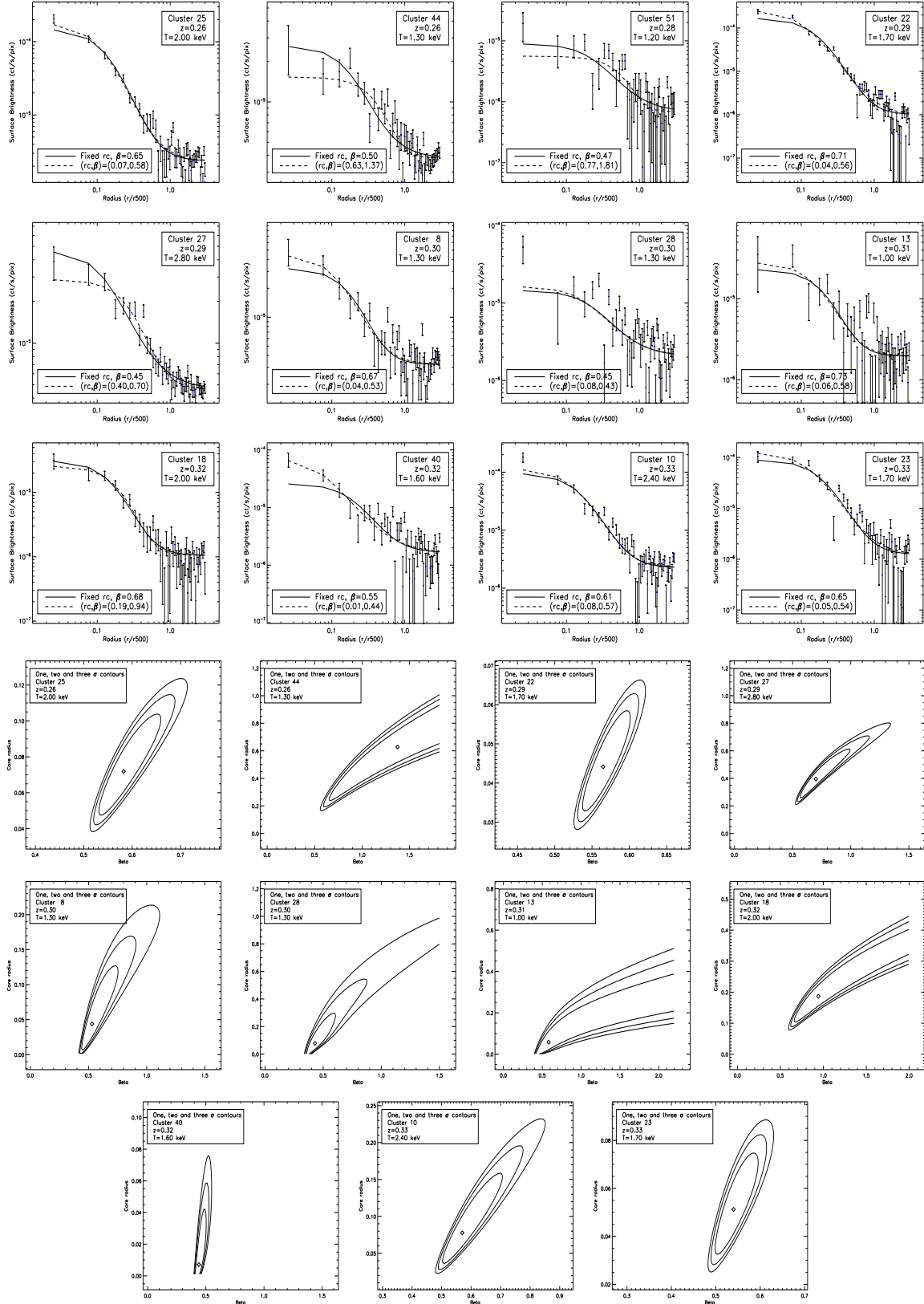


**Figure 2.** X-ray surface brightness profiles of the individual C1 clusters with redshift  $0.26 \leq z \leq 0.33$ , ordered according to redshift and the associated constrained  $1\sigma$ ,  $2\sigma$  and  $3\sigma$  contours. The dashed lines are the fitted  $\beta$ -model profiles with both  $r_{\text{core}}$  and  $\beta$  freely fitted, while the solid lines are for the fitted profiles with free  $\beta$  and  $r_{\text{core}}$  fixed to  $0.105 \times R_{500}$ .

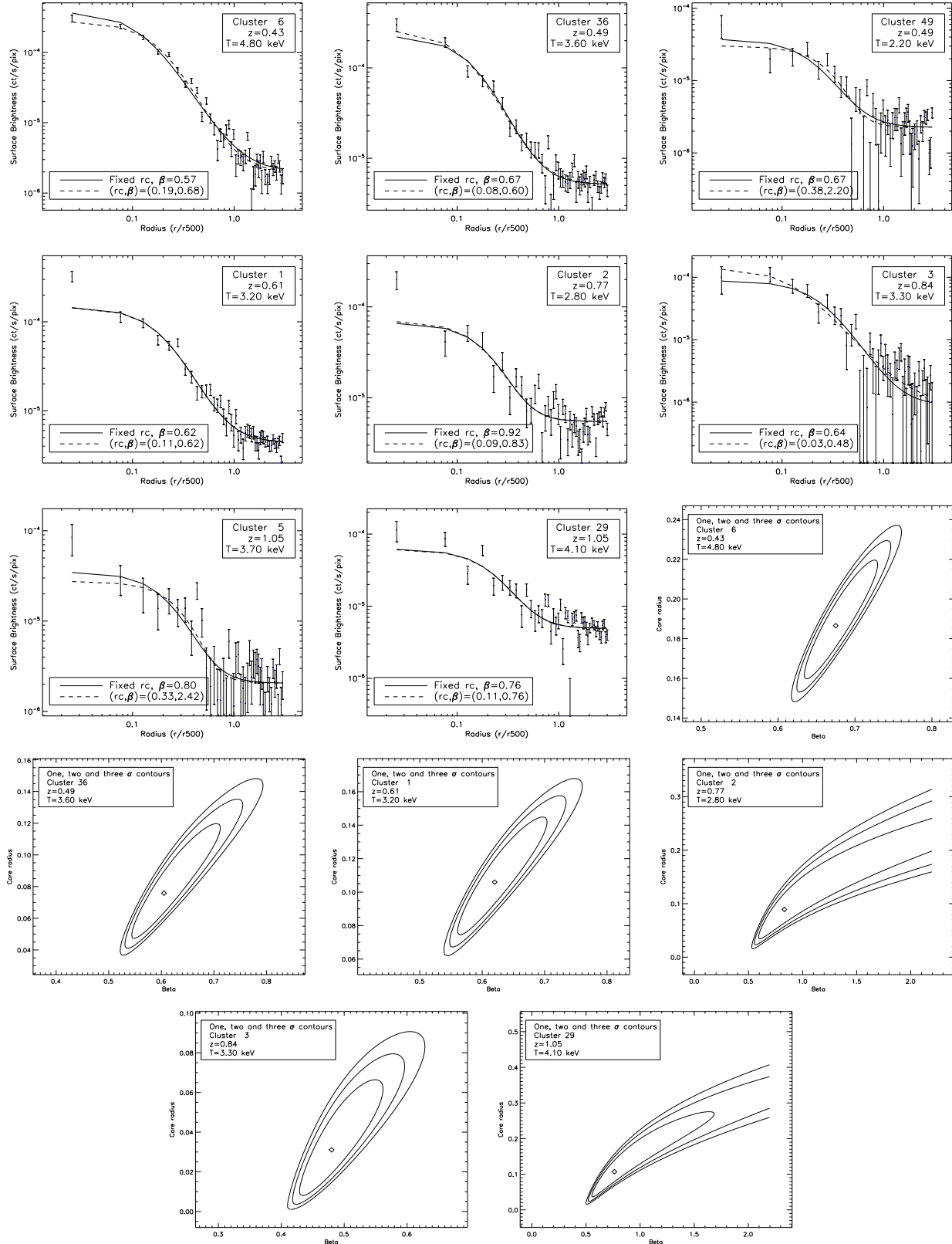


**Figure 3.** X-ray surface brightness profiles of the individual C1 clusters with redshift  $0.43 \leq z \leq 1.05$ , ordered according to redshift and the associated constrained  $1\sigma$ ,  $2\sigma$  and  $3\sigma$  contours. The dashed lines are the fitted  $\beta$ -model profiles with both  $r_{\text{core}}$  and  $\beta$  freely fitted, while the solid lines are for the fitted profiles with free  $\beta$  and  $r_{\text{core}}$  fixed to  $0.105 \times R_{500}$ .



Range	Stacked Clusters XLSSC	Average $z$	Average $kT$ (keV)	$\beta$ Fitted $r_{\text{core}}$	$r_{\text{core}}/R_{500}$	$\beta$ Fixed $r_{\text{core}}$	Central Excess Factor ( $f_c$ )
Redshift-stacked clusters (all clusters)							
$z:0.05-0.17$	11,52,21,41,50,35	0.11	1.33	$0.46^{+0.01}_{-0.01}$	$0.07^{+0.01}_{-0.01}$	$0.49^{+0.003}_{-0.006}$	$1.30 \pm 0.09$
$z:0.26-0.33$	25,44,51,22,27,8,28,13,18,40,10,23	0.30	1.69	$0.51^{+0.01}_{-0.01}$	$0.06^{+0.01}_{-0.01}$	$0.590^{+0.009}_{-0.011}$	$1.56 \pm 0.11$
$z:0.43-1.05$	6,36,49,1,2,47,3,5,29	0.72	3.51	$0.60^{+0.06}_{-0.04}$	$0.07^{+0.02}_{-0.02}$	$0.70^{+0.02}_{-0.03}$	$1.95 \pm 0.25$
Temperature-stacked clusters (all clusters)							
$kT:0.63-1.34$	52,11,21,13,35,51,8,28,44,41	0.20	1.06	$0.49^{+0.03}_{-0.02}$	$0.07^{+0.02}_{-0.02}$	$0.52^{+0.02}_{-0.01}$	$1.48 \pm 0.14$
$kT:1.60-2.80$	40,22,23,18,25,49,10,2,27	0.38	2.13	$0.65^{+0.08}_{-0.05}$	$0.07^{+0.02}_{-0.02}$	$0.79^{+0.03}_{-0.04}$	$2.17 \pm 0.28$
$kT:3.20-4.80$	1,3,50,36,5,47,29,6	0.68	3.76	$0.60^{+0.07}_{-0.05}$	$0.07^{+0.02}_{-0.02}$	$0.69^{+0.02}_{-0.03}$	$1.81 \pm 0.27$
Redshift-stacking for clusters with narrow temperature range: 1.20-1.34 keV							
$z:0.14-0.26$	41,35,44	0.19	1.28	$0.49^{+0.03}_{-0.03}$	$0.10^{+0.03}_{-0.03}$	$0.490^{+0.012}_{-0.008}$	$1.49 \pm 0.18$
$z:0.28-0.30$	51,28,8	0.29	1.27	$0.56^{+0.11}_{-0.07}$	$0.14^{+0.07}_{-0.05}$	$0.52^{+0.02}_{-0.03}$	$1.98 \pm 0.45$
Temperature-stacking for clusters with narrow redshift range: 0.23-0.33							
$kT:1.00-1.60$	13,51,44,28,8,40	0.30	1.28	$0.54^{+0.07}_{-0.04}$	$0.11^{+0.05}_{-0.04}$	$0.53^{+0.02}_{-0.02}$	$1.83 \pm 0.32$
$kT:1.70-2.80$	22,23,25,18,10,27	0.30	2.10	$0.55^{+0.02}_{-0.01}$	$0.07^{+0.01}_{-0.01}$	$0.620^{+0.013}_{-0.006}$	$1.39 \pm 0.10$

**Table 2.** Results of the  $\beta$ -model fit for the redshift-stacked and temperature-stacked clusters for all clusters and for redshift and temperature subsets. The  $\beta$  and  $r_{\text{core}}$  values in the fifth and sixth columns are for the  $\beta$ -model with both  $r_{\text{core}}$  and  $\beta$  freely-fitted. The  $\beta$  values in the seventh column are for the  $\beta$ -model with fixed  $r_{\text{core}}$ . All errors are  $1\sigma$  errors.

in agreement with studies of low redshift groups (see for example, Helsdon & Ponman 2000 and Mulchaey et al. 2003). Helsdon & Ponman (2000) attributed the fact that the slopes of group surface brightness profiles are flatter than the canonical slope ( $\beta=0.67$ ) for clusters, as a result of the effects of feedback from galactic winds on the intergalactic medium. The stacked data show a central excess, with  $f_c = 1.56 \pm 0.11$ , indicating that these systems typically possess CCs. The individual profiles of  $z \sim 0.3$  clusters in Fig. 2, also support this result; the central excess factor,  $f_c$  is greater than unity for 7 of the 12 clusters (25,51,22,8,28,40 and 10) and an additional 4 clusters (44,13,18 and 23) have best fit  $f_c > 1$ , but with error bars crossing unity. So, we conclude that 58-92% of our systems at  $z \sim 0.3$  have CCs. The fitted  $r_{\text{core}}$  for the stacked profiles is  $0.06 \times R_{500}$ .

## 4.2 Trends of $f_c$ and $\beta$ with redshift and temperature

The main results of our analysis are the presence of trends in the value of  $\beta$ , and in the incidence of cuspy cores, with redshift and temperature. Our C1 clusters, as for any deep cluster survey, suffer from *Malmquist* selection effects, which result in increasing mean cluster luminosity with redshift, due to the fact that higher redshift clusters are more difficult to detect than nearby ones – see Fig. 3 in Pacaud et al. (2007). Given the well-known correlation between X-ray luminosity and temperature, there is a corresponding tendency for more distant clusters in our sample to be hotter. This correlation between  $z$  and  $T$  within our sample, makes it difficult to establish whether our observed trends in  $\beta$  and  $f_c$  are evolutionary effects, or whether they represent changes in cluster properties with system mass (and hence temperature).

We attempt to address this issue in two ways: firstly, we can examine whether the trends we see (in both individual and stacked clusters) are stronger with respect to  $T$  or  $z$ . Secondly, we use the group of clusters at  $z \sim 0.3$ ; subdividing these by temperature allows us to check for trends with  $T$  at essentially a single redshift.

Similarly, we also extract a subset of our clusters which cover a rather narrow temperature range, but a larger spread in  $z$ .

### 4.2.1 Trends of $f_c$

To investigate whether the trends we see in the redshift-stacked sets are affected by the  $T$ - $z$  correlation in our sample, we select six clusters with similar temperatures ( $kT=1.20$  to  $1.34$  keV) but a relatively wide spread in redshift ( $z=0.14$  to  $0.30$ ). These are then divided into two subsets, each consisting of three systems: the first has  $0.14 \leq z \leq 0.26$  (average  $z=0.19$ ) and mean temperature  $\overline{kT}=1.28$  keV, the second has  $0.28 \leq z \leq 0.30$  (average  $z = 0.29$ ) and  $\overline{kT}=1.27$  keV. The fit results for these subsets are shown in Fig. 6 and in Table 2.

Similarly, we divided the twelve  $z \sim 0.3$  clusters, which span a temperature range of  $1.0$ - $2.8$  keV, into two temperature bins:  $1.0$ - $1.6$  keV and  $1.7$ - $2.8$  keV with six clusters in each. See Fig. 7 and the last two rows in Table 2 for the results of stacking these subsets. The  $1.0$ - $1.6$  keV clusters have an average redshift  $z = 0.30$  and average temperature  $\overline{kT}=1.28$  keV, while the  $1.7$ - $2.8$  keV clusters have the same average redshift  $z = 0.30$  and  $\overline{kT}=2.1$  keV.

The results from these subsets, shown in Fig. 6 and 7, reinforce the impression from Fig. 4 and 5 that the increase in profile cusps is a function of  $z$  rather than  $T$ . In fact, the temperature-stacked subset (Fig. 7) actually shows a *decline* in  $f_c$  with temperature, whilst in the redshift-stacked subset it increases from  $1.49$  for the  $0.14 \leq z \leq 0.26$  clusters to  $1.98$  for the  $0.28 \leq z \leq 0.30$  clusters (Fig. 6).

We also tested the  $f_c$ - $z$  behaviour in the individual profiles. In Fig. 8, we plot  $f_c$  against redshift for the individual C1 clusters. The figure shows that the high- $z$  clusters tend to have larger-than-unity values of  $f_c$  more often than clusters at lower redshift. We tested for a correlation in this plot, using the Pearson correlation coefficient, which has a value  $0.40$  for  $26$  points, corresponding to a Student  $t$  value of  $2.12$ , which shows a positive correlation at

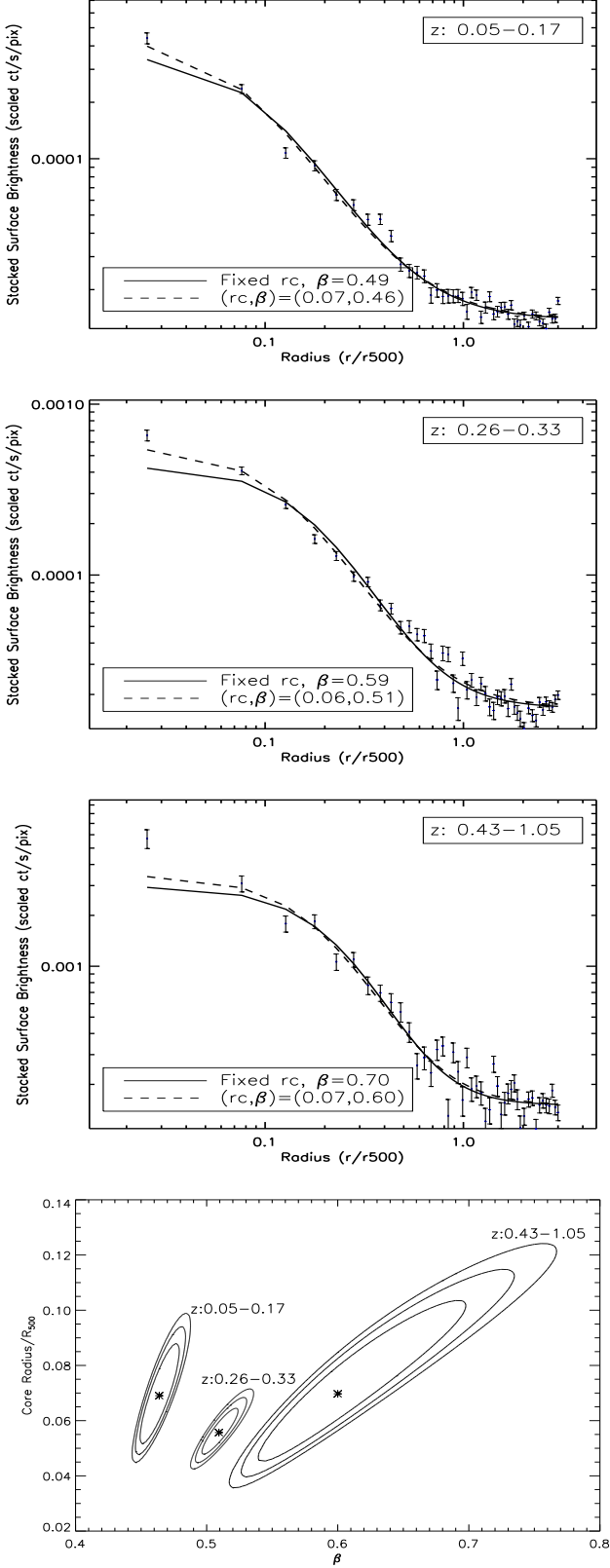


**Figure 4.** X-ray surface brightness profiles of the redshift-stacked C1 clusters with the associated  $1\sigma$ ,  $2\sigma$  and  $3\sigma$  contours of the free  $r_{\text{core}}$  fit. The dashed lines are the fitted  $\beta$ -model profiles with both  $r_{\text{core}}$  and  $\beta$  freely fitted, while the solid lines are for the fitted profiles with free  $\beta$  and  $r_{\text{core}}$  fixed to  $0.105 \times R_{500}$ .

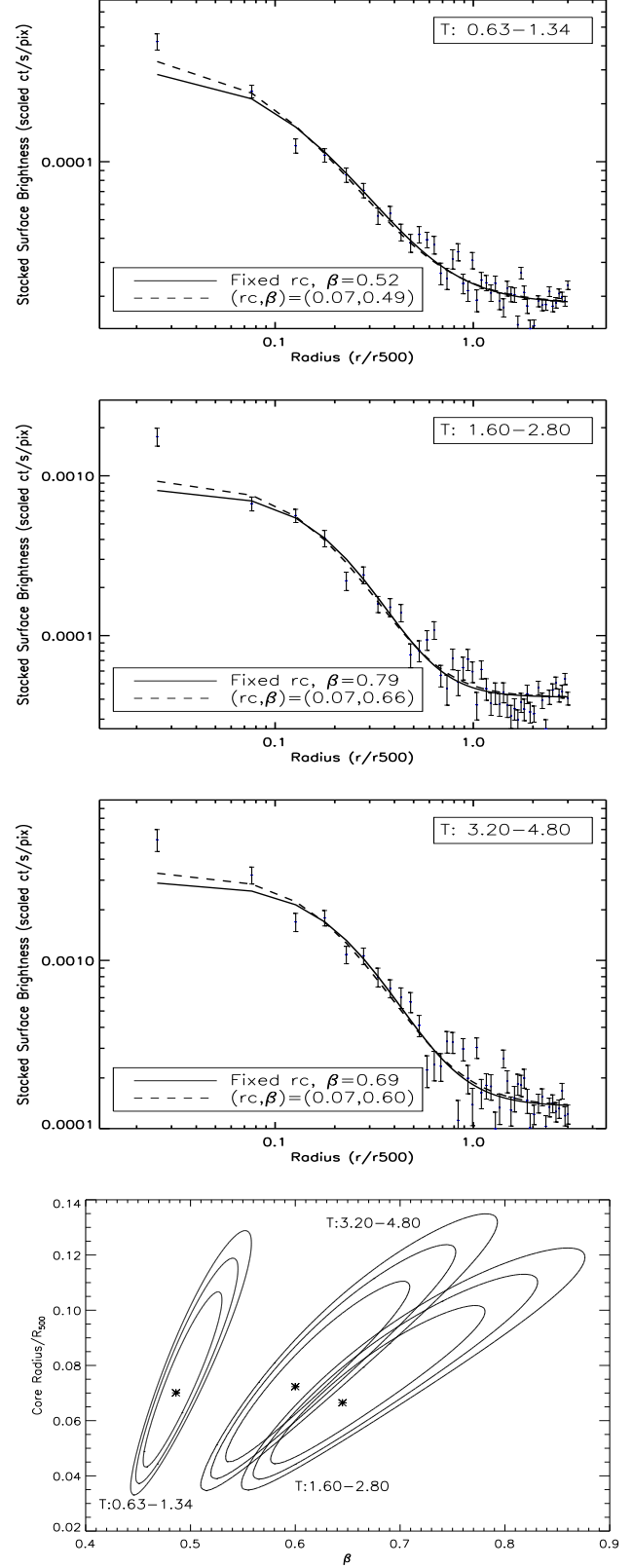


**Figure 5.** X-ray surface brightness profiles of the temperature-stacked C1 clusters with the associated  $1\sigma$ ,  $2\sigma$  and  $3\sigma$  contours of the free  $r_{\text{core}}$  fit. The dashed lines are the fitted  $\beta$ -model profiles with both  $r_{\text{core}}$  and  $\beta$  freely fitted, while the solid lines are for the fitted profiles with free  $\beta$  and  $r_{\text{core}}$  fixed to  $0.105 \times R_{500}$ .

over 95% significance (2-tailed test). To visualise the trend more clearly, we grouped adjacent data points into three bins and computed their weighted mean and the standard error. These binned results are shown as diamonds, though it should be noted that resulting values are sensitive to the choice of bin boundaries.

In contrast, the  $f_c$ -temperature plot in Fig. 9, shows no monotonic trend in  $f_c$  with  $T$ , with a Pearson correlation coefficient of 0.01. The binned values (diamonds) agree well the temperature-stacked results discussed earlier, where we noticed that intermediate-temperature clusters had the highest central excess.

The present work is the first study of the *evolution* of CCs within galaxy groups, although previous work (e.g., Helsdon & Ponman 2000) has shown that CCs are common in X-ray bright groups at low redshift. Richer clusters have received much more study. CC clusters are found to be common at low and moderate redshifts, see Bauer et al. (2005), but Vikhlinin et al. (2007) found only a very small fraction of clusters at  $z > 0.5$  to have cuspy X-ray brightness profiles, which were taken as an indication of cool cores. Santos et al. (2008) found moderate CC clusters out to  $z = 1.4$ , but noted an absence of *strong* CCs at redshifts higher than 0.7.

Our results therefore suggest that groups behave differently to clusters, in that cuspy cores are actually *more* prominent at higher  $z$  in these poorer systems. How can we understand this difference? One possibility is that the central excess seen in groups at moderate-high  $z$  is not due to CCs at all, but to the presence of central AGN. We can immediately rule out the possibility that the effect is due to just a few groups with bright AGN contaminating our stacked profiles by noting (cf. Fig. 8) that a central excess is seen in the *majority* of systems at  $z > 0.3$ . Hence, any effect from central AGN would have to be widespread and moderate.

There would be significant spectral differences between central excesses generated by CCs and AGN, since the thermal emission from cool cores is much softer than the X-ray spectra of AGN. The limited statistics for individual clusters in our sample do not permit us to investigate whether the core emission is soft or hard. However, this can be investigated using the stacked data. We therefore repeated the stacking analysis for intermediate- and high- $z$  clusters using X-ray images derived from the hard energy band, 2.0–4.5 keV. The results are shown in Fig. 10. Comparing with the corresponding soft (0.5–2.0 keV) band profiles in Fig. 4, we notice the disappearance of the central excess above the  $\beta$ -model in the hard-energy profiles in both the intermediate and high redshift stacks. This provides strong evidence that this central excess does not arise from AGN in cluster cores.

Assuming that the cuspy profiles really do indicate the presence of CCs, the observation of such cores in groups at high redshift can help to constrain the reasons for their absence in high  $z$  clusters. The decline in CC clusters with redshift could result from disruption of CCs due to the higher merging rates at high redshifts (e.g., Cohn & White 2005 and Jeltima et al. 2005) or from the effects of preheating (McCarthy et al. 2004), which can raise the gas entropy and prevent cooling. In the latter case, the impact of a given entropy boost will be larger in cooler systems (see e.g. Borgani et al. 2005), especially at high redshift, so one would expect if anything to see a *drop* in the incidence of CCs within groups at high  $z$ , at least as large as pronounced as that in richer clusters.

The hypothesis that CCs are destroyed by cluster mergers appears more promising, since this effect might be stronger in more massive systems. For example, Burns et al. (2008) find that CCs are more common in low mass clusters, and attribute the lack of CCs in

more massive systems to their destruction by early mergers in systems destined to grow into large clusters. On the other hand, these authors caution that their model does not reproduce the observed reduction with redshift in CCs within massive clusters. In fact, no numerical simulations have yet succeeded in adequately reproducing the properties of cluster cores.

#### 4.2.2 Trends of $\beta$

Whilst it seems quite clear, as discussed above, that the trend in central cuspsiness is primarily related to redshift, rather than temperature, the situation with regard to  $\beta$  is not so straightforward. In the stacked datasets, comparison of Fig. 4 and 5 suggest that the relationship with redshift is stronger:  $\beta$  rises monotonically through the three redshift intervals, whilst in temperature the only clear result is that the cool systems have lower  $\beta$ . In contrast, the fits to individual clusters (Fig. 11 and 12) show a more pronounced trend with temperature than with redshift. The stacked subsets of the narrow temperature and redshift ranges (Fig. 7 and 6) produce ambiguous results:  $\beta$  increases with temperature if  $r_{\text{core}}$  is fixed, but with  $z$  if  $r_{\text{core}}$  is left free to fit.

So, on the basis of our data alone, we are unable to say whether the general trend in  $\beta$  is driven by the temperature or the redshift. However, evidence from studies of low redshift groups and clusters is very relevant here. Such studies provide clear evidence of a positive correlation between  $\beta$  and temperature in local systems – e.g., Osmond & Ponman (2004) and Fig. 7 in the study of Croston et al. (2008), who analysed clusters with redshift  $< 0.2$ . Combining these previous results with ours, favours a trend in  $\beta$  with temperature (and hence cluster mass) rather than an evolutionary effect. Our results then demonstrate that this trend is still present in groups and clusters at  $z \sim 0.3$ .

## 5 SUMMARY AND CONCLUSIONS

In this paper, we used *XMM-Newton* observations of 27 X-ray selected galaxy clusters spanning the redshift range ( $0.05 \leq z \leq 1.05$ ) to study the spatial properties of their ICM. Most of these clusters fall in the realm of low-mass clusters or groups, with ICM temperatures from 0.63 to 4.80 keV. The XMM data provide typically a few hundreds X-ray source counts. We extracted and vignetting-corrected the profiles to  $3 \times R_{500}$  where they flattened and reached the photon background values, which were estimated locally for each cluster.

In addition to the individual profiles, we also stacked the profiles into three redshift and temperature bins. To explore the effects of *Malmquist bias*, we further stacked clusters with similar redshifts/temperatures into two subsets each with different averaged temperature/redshift. Both individual and stacked profiles were fitted with blurred (to account for the PSF errors of the *XMM-Newton* cameras)  $\beta$ -models with both free and fixed core radii. The fixed- $r_{\text{core}}$   $\beta$ -model fits were used to test whether a profile showed evidence of a cuspy core, making this study the first to probe the evolution of CCs out to  $z \gtrsim 0.3$  within poor clusters.

Our main conclusions are:

- We find that 54% of our sample show evidence for cool cores, in the form of a central excess (at  $> 1\sigma$  significance) above a standard  $\beta$ -model.
- For the free- $r_{\text{core}}$  fits to individual clusters, the median value of  $\beta$  is 0.61, and the median  $r_{\text{core}}$  is  $0.08 \times R_{500}$ .

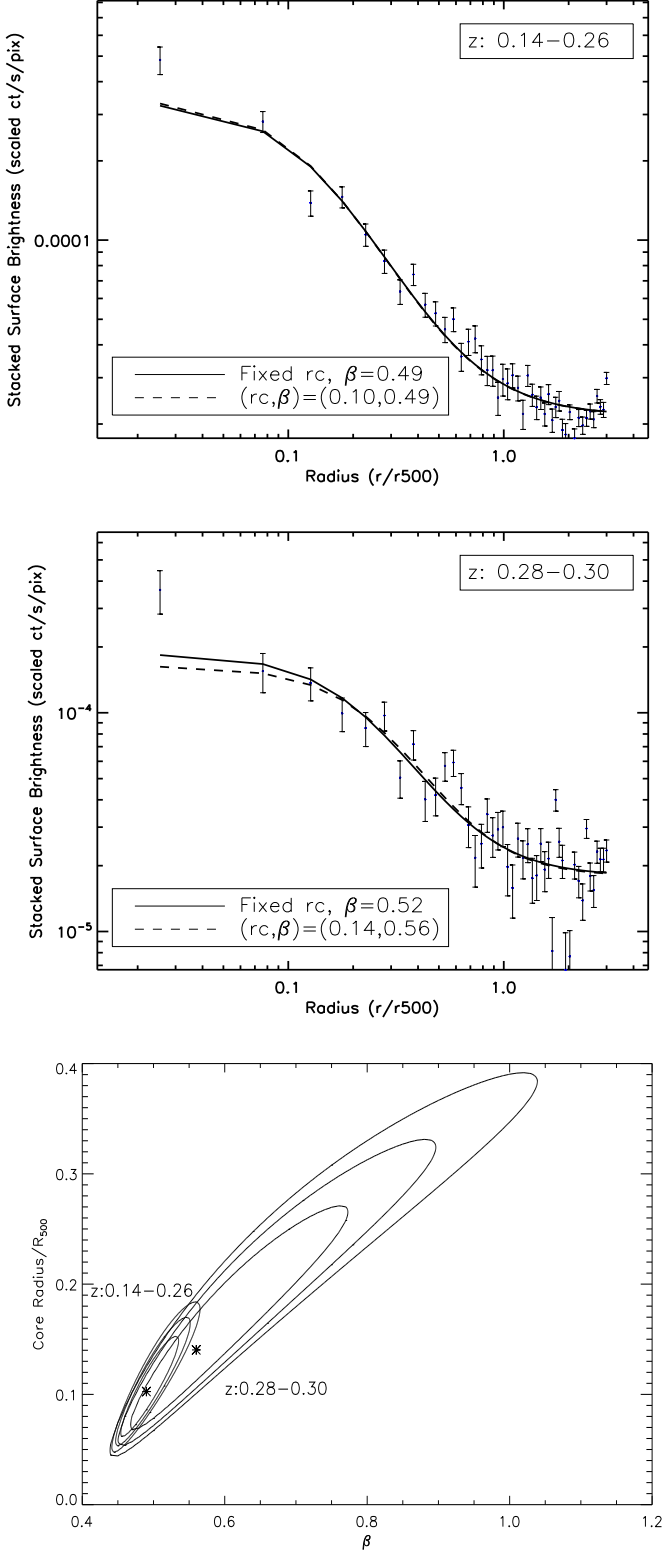


**Figure 6.** X-ray surface brightness profiles of stacked C1 clusters with narrow temperature range (1.20–1.34 keV), grouped into two redshift bins:  $0.14 \leq z \leq 0.26$  (top panel) and  $0.28 \leq z \leq 0.30$  (middle panel). The bottom panel is the  $1\sigma$ ,  $2\sigma$  and  $3\sigma$  contours. The dashed lines are the fitted  $\beta$ -model profiles with both  $r_{\text{core}}$  and  $\beta$  freely fitted, while the solid lines are for the fitted profiles with free  $\beta$  and  $r_{\text{core}}$  fixed to  $0.105 \times R_{500}$ .

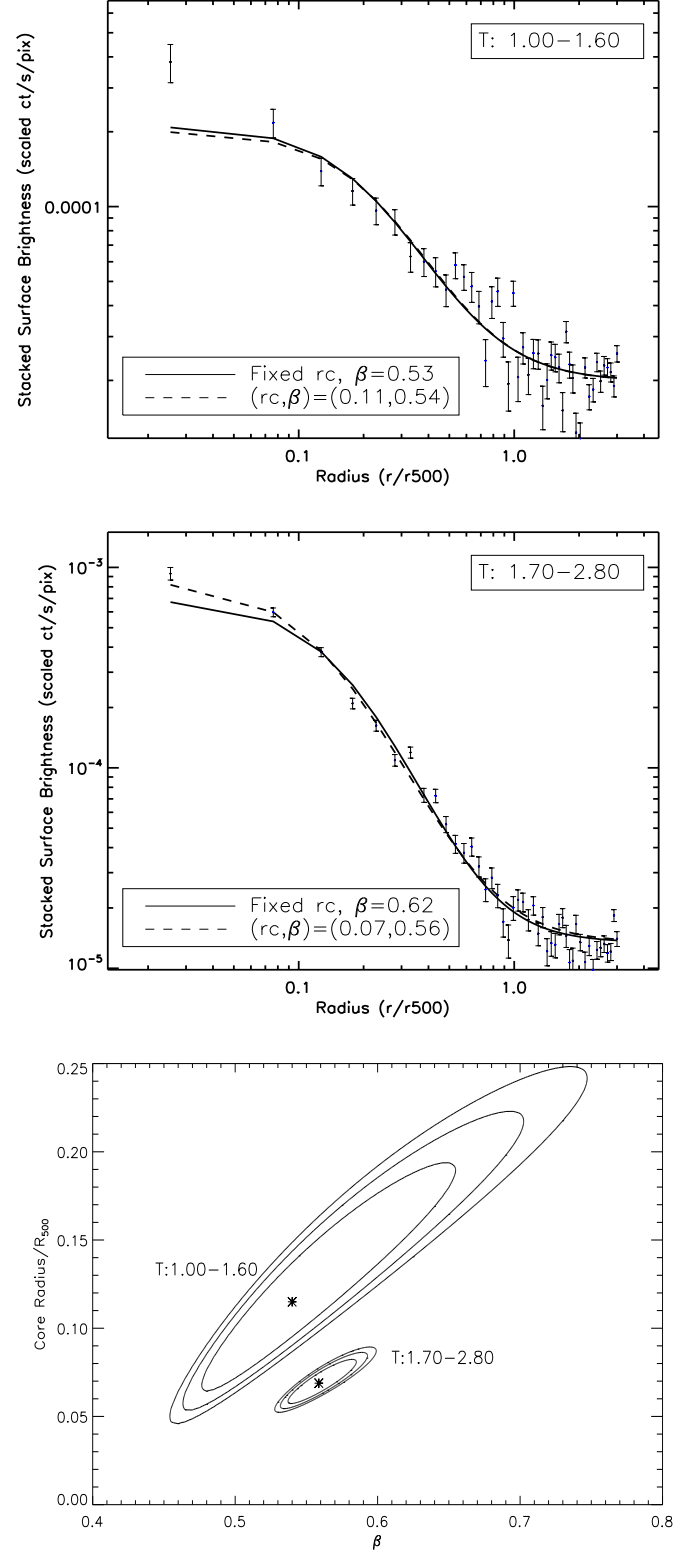


**Figure 7.** X-ray surface brightness profiles of stacked C1 clusters with narrow redshift range (0.23–0.33), grouped into two temperature bins: 1.00–1.60 keV (top panel) and 1.70–2.80 keV (middle panel). The bottom panel is the  $1\sigma$ ,  $2\sigma$  and  $3\sigma$  contours. The dashed lines are the fitted  $\beta$ -model profiles with both  $r_{\text{core}}$  and  $\beta$  freely fitted, while the solid lines are for the fitted profiles with free  $\beta$  and  $r_{\text{core}}$  fixed to  $0.105 \times R_{500}$ .

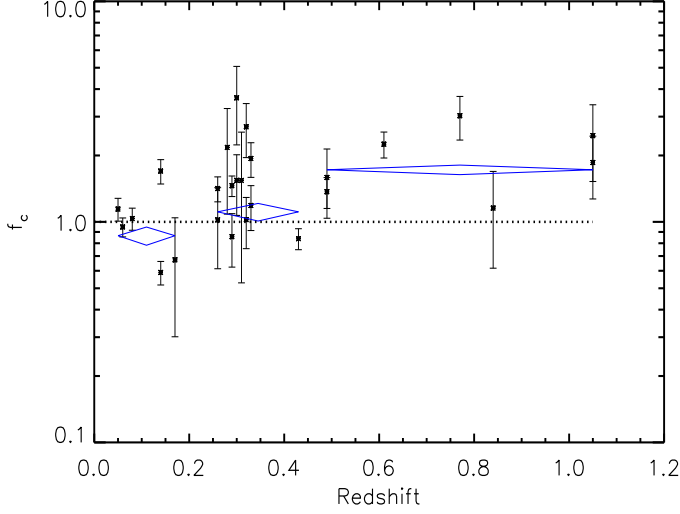


**Figure 8.** Central excess factor,  $f_c$  (of the fixed  $r_{\text{core}}$  fits) plotted against redshift of the individual C1 clusters.  $f_c$  is defined as the ratio of the observed surface brightness to the predicted (model) surface brightness within  $0.02 \times R_{500}$  (first radial bin). A value of  $f_c$  above 1 is an indication of a cool core cluster and vice versa. The positions and sizes of the diamonds represent the weighted means and the standard errors of the weighted means of the points as described in text and appendix A.

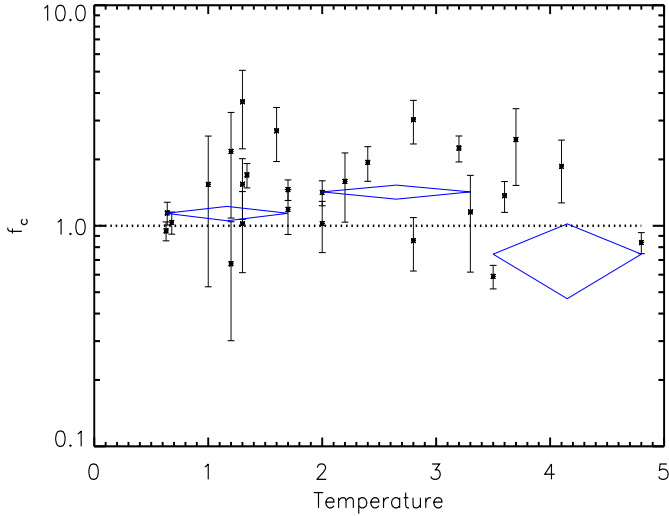


**Figure 9.** Central excess factor,  $f_c$  (of the fixed  $r_{\text{core}}$  fits) plotted against temperature of the individual C1 clusters. The positions and sizes of the diamonds are calculated as described in appendix A.

- For the fixed- $r_{\text{core}}$  fits to individual clusters, the median  $\beta$  is 0.63.

- Twelve systems in our sample (with  $\overline{kT} = 1.69$  keV) have  $z \sim 0.3$ , allowing us to characterise the X-ray surface brightness profiles of intermediate redshift X-ray selected groups. The free-fit parameters to the stacked data from these 12 systems gives  $\beta = 0.51 \pm 0.01$  and  $r_{\text{core}} = 0.06 \pm 0.01 \times R_{500}$ . This stacked profile indicates the presence of CCs ( $f_c = 1.56 \pm 0.11$ ), with 7 of the 12 systems showing a significant central excess in their individual profiles.

- Stacked and individual profiles for our sample of poor galaxy clusters show that the CCs do not disappear at high redshift, but

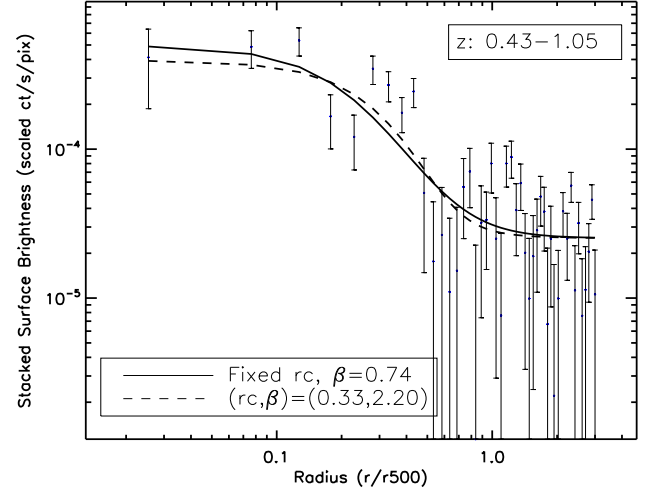
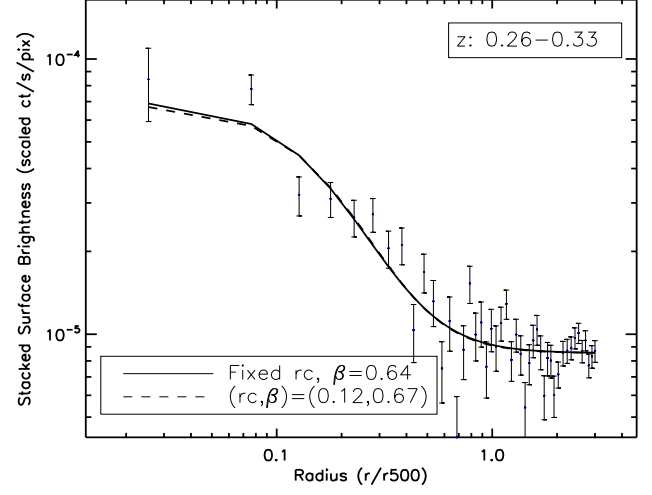


**Figure 10.** Stacked profiles for the intermediate- and high-redshift cluster subsamples extracted from hard band (2.0-4.5 keV). These can be compared directly with the corresponding soft band stacks shown in Fig. 4, and shown that the central excess above the fixed- $r_{\text{core}}$   $\beta$ -model is not present in the hard band.

rather become more prominent, though one would like to confirm this result with higher spatial resolution observations.

- The slope parameter,  $\beta$ , shows a positive trend with both redshift and temperature in our data. Combining this results with previous findings, we incline towards a trend with temperature (and hence mass) rather than redshift. The present study then demonstrates for the first time, that the  $\beta$ - $T$  trend seen at low  $z$  is also present in groups and clusters at  $z \gtrsim 0.3$ .

## 6 ACKNOWLEDGEMENTS

We thank Monique Arnaud for providing us with the FORTRAN code which was used to calculate the point spread function redistribution matrix, and Ewan O’Sullivan for useful discussions about AGN contamination in cluster cores. XMM-Newton is an ESA observatory.

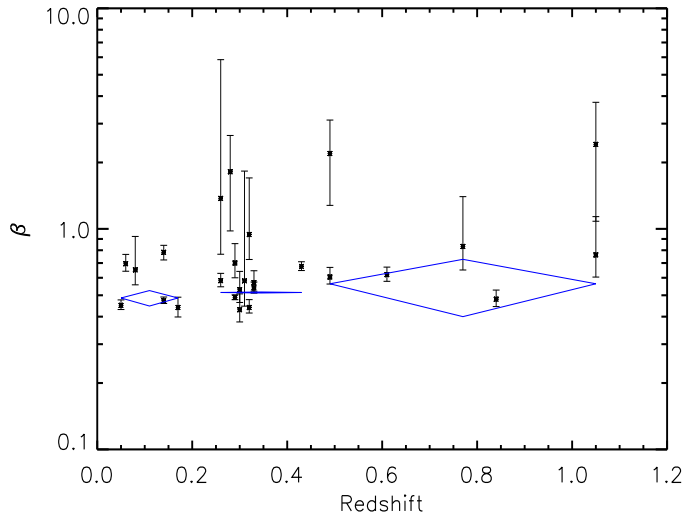


**Figure 11.**  $\beta$  values (of the free  $r_{\text{core}}$  fits) versus redshift of the individual C1 clusters. The positions and sizes of the diamonds are calculated as described in appendix A.

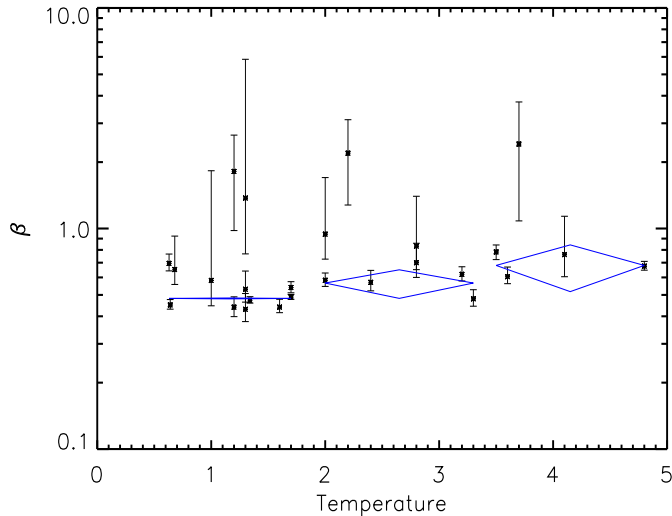


**Figure 12.**  $\beta$  values (of the free  $r_{\text{core}}$  fits) versus temperature of the individual C1 clusters. The positions and sizes of the diamonds are calculated as described in appendix A.

## REFERENCES

- Arnaud M. et al., 2002, *A&A*, 390, 27  
 Bauer F. E., Fabian A. C., Sanders J. S., Allen S. W., Johnstone R. M., 2005, *MNRAS*, 359, 1481  
 Bahcall J. N., Sarazin C. L., 1977, *ApJ*, 213, L99  
 Borgani S., Finoguenov A., Kay S. T., Ponman T. J., Springel V., Tozzi P., Voit G. M., 2005, *MNRAS*, 361, 233  
 Branduardi-Raymont G., Fabricant D., Feigelson E., Gorenstein P., Grindlay J., Soltan A., Zamorani G., 1981, *ApJ*, 248, 55  
 Burns J. O., Hallman E. J., Gantner B., Motl P. M., Norman M. L., 2008, *ApJ*, 675, 1125  
 Cavaliere A., Fusco-Femiano R., 1976, *A&A*, 49, 137  
 Chen Y., Reiprich T. H., Böhringer H., Ikebe Y., Zhang Y.-Y., 2007, *A&A*, 466, 805  
 Cohn J. D., White M., 2005, *Astropart. Phys.*, 24, 316  
 Croston J. H. et al., 2008, *A&A*, 487, 431  
 Donahue M., Voit G. M., 2004, in Mulchaey J. S., Dressler A., Oemler A., eds, *Clusters of Galaxies: Probes of Cosmological Structure and Galaxy Evolution*, Cool Gas in Clusters of Galaxies. Cambridge University Press, Cambridge, UK, p. 143  
 Edge A. C., Stewart G. C., Fabian A. C., 1992, *MNRAS*, 258, 177  
 Ettori S. et al., 2004, *MNRAS*, 354, 111  
 Fabian A. C., 1994, *ARA&A*, 32, 277  
 Finoguenov A. et al., 2007, *ApJS*, 172, 182  
 Finoguenov A., Reiprich T. H., Böhringer H., 2001, *A&A*, 368, 749  
 Gorenstein P., Fabricant D., Topka K., Harnden F. R., Jr, Tucker W. H., 1978, *ApJ*, 224, 718  
 Helsdon S. F., Ponman T. J., 2000, *MNRAS*, 315, 356  
 Hinshaw G. et al., 2009, *ApJS*, 180, 225  
 Horner, D. J., R. F. Mushotzky, and C. A. Scharf, 1999, *Astrophys. J.* 520, 78  
 Jeltema T. E., Canizares C. R., Bautz M. W., Buote D. A., 2005, *ApJ*, 624, 606  
 Jeltema T. E. et al., 2009, *MNRAS*, 399, 715  
 Jeltema T. E., Mulchaey J. S., Lubin L. M., Fassnacht C. D., 2007, *ApJ*, 658, 865  
 Jeltema T. E., Mulchaey J. S., Lubin L. M., Rosati P., Böhringer H., 2006, *ApJ*, 649, 649  
 Jones C., Forman W., 1984, *ApJ*, 276, 38  
 Kay S. T., da Silva A. C., Aghanim N., Blanchard A., Liddle A. R., Puget J.-L., Sadat R., Thomas P. A., 2007, *MNRAS*, 377, 317  
 Maughan B. J., Jones C., Forman W., Van Speybroeck L., 2008, *ApJS*, 174, 117  
 McCarthy I. G., Balogh M. L., Babul A., Poole G. B., Horner D. J., 2004, *ApJ*, 613, 811  
 Mulchaey J. S., Davis D. S., Mushotzky R. F., Burstein D., 2003, *ApJS*, 145, 39  
 Mulchaey J. S., Lubin L. M., Fassnacht C., Rosati P., Jeltema T. E., 2006, *ApJ*, 646, 133  
 Neumann D. M., Arnaud M., 1999, *A&A*, 348, 711  
 Osmond J. P. F., Ponman T. J., 2004, *MNRAS*, 350, 1511  
 Ota N., Mitsuda K., 2004, *A&A*, 428, 757  
 Pacaud F. et al., 2006, *MNRAS*, 372, 578  
 Pacaud, F., et al. 2007, *MNRAS*, 382, 1289  
 Peres C. B., Fabian A. C., Edge A. C., Allen S. W., Johnstone R. M., White D. M., 1998, *MNRAS*, 298, 416  
 Peterson J. R., Fabian A. C., 2006, *Phys. Rep.*, 427, 1  
 Ponman T. J., Sanderson A. J. R., Finoguenov A., 2003, *MNRAS*, 343, 331  
 Pratt G. W., Arnaud M., 2002, *A&A*, 394, 375  
 Rasmussen J., Ponman T. J., 2004, *MNRAS*, 349, 722  
 Santos J. S., Rosati P., Tozzi P., Böhringer H., Ettori S., Bignamini A., 2008, *A&A*, 483, 35  
 Sarazin C. L., 1986, *Rev. Mod. Phys.*, 58, 1  
 Schuecker P., Böhringer H., Reiprich T. H., Feretti L., 2001, *A&A*, 378, 408  
 Strüder L. et al., 2001, *A&A*, 365, L18  
 Sun M., Voit G. M., Donahue M., Jones C., Forman W., Vikhlinin A., 2009, *ApJ*, 693, 1142  
 Tolman R. C., 1930, *Proc. Natl. Acad. Sci.*, 16, 511  
 Turner M. J. L. et al., 2001, *A&A*, 365, L27  
 Vikhlinin A., Burenin R., Forman W. R., Jones C., Hornstrup A., Murray S. S., Quintana H., 2007, in Böhringer H., Pratt G. W., Finoguenov A., Schuecker P., eds, *Heating versus Cooling in Galaxies and Clusters of Galaxies*. Springer, Berlin, p. 48  
 Vikhlinin A., Forman W., Jones C., 1999, *ApJ*, 525, 47

Voit G. M., 2005, Rev. Mod. Phys., 77, 207  
 Willis J. P. et al., 2005, MNRAS, 363, 675  
 Wilman D. J., et al., 2005, MNRAS, 358, 88  
 White D. A., Jones C., Forman W., 1997, MNRAS, 292, 419  
 Zabludoff A. I., Mulchaey J. S., 1998, ApJ, 496, 39

## APPENDIX A: STANDARD ERROR ON WEIGHTED MEAN IN PRESENCE OF REAL SCATTER

When averaging data of variable statistical quality, a more robust mean is obtained by weighting the averaged values by their inverse variances. Standard formulae for the standard error on such a weighted mean assume that statistical errors represent the *only* source of variance. For our application, this is not true, since there are real cluster-to-cluster variations, in addition to statistical scatter. Here we derive an expression for the standard error of a weighted mean in these circumstances.

For a data set  $x_i = x_1, x_2, \dots, x_n$  with variable statistical errors  $\sigma_i = \sigma_1, \sigma_2, \dots, \sigma_n$ , the weighted mean  $\bar{x}$  is

$$\bar{x} = \frac{\sum_{i=1}^n w_i x_i}{\sum_{i=1}^n w_i}, \quad (\text{A1})$$

where  $w_i = 1/\sigma_i^2$  are the weights. This weighted mean will properly take into account the varying statistical quality of the data.

The variance in this the weighted mean,  $\text{var}(\bar{x})$ , is

$$\text{var}(\bar{x}) = \frac{\sum_{i=1}^n w_i^2 \text{var}(x_i)}{\left(\sum_{i=1}^n w_i\right)^2}. \quad (\text{A2})$$

In the presence of real, non-statistical scatter in the  $x$  values, the expected variance for the  $i$ th data point is

$$\text{var}(x_i) = \langle (x_i - \mu)^2 \rangle = \sigma_i^2 + \sigma_t^2, \quad (\text{A3})$$

where  $\sigma_t$  is the *true* (non-statistical) variance of the population and

$$\langle (x_i - \mu)^2 \rangle = \frac{n}{n-1} \langle (x_i - \bar{x})^2 \rangle. \quad (\text{A4})$$

So an estimate  $\hat{\sigma}_t^2$  of  $\sigma_t^2$  is obtained from

$$\hat{\sigma}_t^2 = \frac{1}{n-1} \sum_{i=1}^n [(x_i - \bar{x})^2 - \sigma_i^2], \quad (\text{A5})$$

and the variance of the weighted mean becomes

$$\text{var}(\bar{x}) = \frac{\sum_{i=1}^n w_i^2 \left[ \sigma_i^2 + \frac{1}{n-1} \sum_{i=1}^n [(x_i - \bar{x})^2 - \sigma_i^2] \right]}{\left(\sum_{i=1}^n w_i\right)^2}. \quad (\text{A6})$$

Substituting for  $w_i = 1/\sigma_i^2$  we get

$$\text{var}(\bar{x}) = \frac{\sum_{i=1}^n \left[ \frac{1}{\sigma_i^2} + \frac{\hat{\sigma}_t^2}{\sigma_i^4} \right]}{\left(\sum_{i=1}^n \frac{1}{\sigma_i^2}\right)^2}, \quad (\text{A7})$$

and finally the standard error of the weighted mean (SEWM),  $SE_{\bar{x}}$ , is

$$SE_{\bar{x}} = \sqrt{\frac{\text{var}(\bar{x})}{n}} = \sqrt{\frac{\sum_{i=1}^n \left[ \frac{1}{\sigma_i^2} + \frac{\hat{\sigma}_t^2}{\sigma_i^4} \right]}{n \left(\sum_{i=1}^n \frac{1}{\sigma_i^2}\right)^2}}. \quad (\text{A8})$$

This paper has been typeset from a  $\text{\TeX}/\text{\LaTeX}$  file prepared by the author.